(Received 20 March 2026, Accepted 27 April 2026, Scheduled 7 June 2026)

Analytical Modeling and Full-Wave Simulation of Metal and Dielectric Trihedral Corner Reflectors and Their Arrays

Denys I. Zaikin*

Whitecell Systems ApS, Lyngvej 8, Aalborg 9000, Denmark

ABSTRACT: This work presents a unified analytical and full-wave investigation of the monostatic radar cross section (RCS) of trihedral corner reflectors (TCRs) and their arrays, covering both metallic and dielectric configurations. Accurate analytical prediction of the monostatic RCS of trihedral corner reflector arrays (TCRAs), particularly for tightly packed mosaic geometries and dielectric materials, remains challenging due to the lack of general closed-form models accounting for multiple reflector orientations and array effects. To address this gap, closed-form RCS expressions are derived for single reflectors and mosaic arrays incorporating two distinct reflector orientations. The proposed formulation extends classical geometrical-optics models through a corrected complex-target phase treatment and explicit inclusion of multi-orientation effects. The analytical results are validated using full-wave finite-element simulations in COMSOL Multiphysics®. For metallic reflectors, geometrical optics is shown to be accurate for electrically large elements, whereas diffraction, resonance, and phase-distortion effects emerge as the reflector size decreases. Dielectric TCRAs exhibit strongly non-symmetrical scattering and reversed boresight offsets in the $\varphi = \pi/2$ plane; nevertheless, grating-lobe locations remain predictable using the metal-array analytical model. The study concludes with practical design guidelines for mosaic TCRAs, including peak-RCS scaling, grating-lobe placement, and the transition from corner-reflector to plate-like scattering.

1. INTRODUCTION

Trihedral corner reflectors (TCRs) and their arrays are fundamental elements in radar engineering, serving as calibration standards for RCS measurement systems, reference targets for automotive and remote-sensing radars, and building blocks for retroreflective metasurfaces. As modern radar platforms increasingly operate at millimeter-wave frequencies and utilize large, densely packed scatterer arrays, the ability to accurately predict the monostatic radar cross section (RCS) of both metallic and dielectric TCRs — over a wide range of electrical sizes and array configurations — has become technologically critical. Reliable analytical tools are required to reduce the dependence on full-wave simulations, accelerate design cycles, and enable the accurate calibration of high-resolution sensing systems. These capabilities are essential for the design, verification, and performance assessment of next-generation radar sensors, including automotive, airborne, and ground-based systems. The present work focuses on the prediction of monostatic RCS magnitude using a scalar formulation; full polarimetric or scattering-matrix analysis is beyond the scope of this study.

While the polarimetric characteristics of trihedral reflectors are central to many calibration applications, a qualitative discussion of polarization effects is included only to clarify the applicability and limitations of the proposed scalar analytical model.

Despite their importance, existing research on TCRAs is limited in scope. Recent studies have examined advanced reflector geometries and fabrication methods [1–3], high-frequency and quasi-omnidirectional behaviors [4], and dynamic or airborne reflector configurations [5]. These works highlight the modern applications of TCR-based structures and demonstrate the continued relevance of reflector research at millimeter-wave frequencies. Recent studies have further explored high-frequency analytical modeling of trihedral corner reflectors and array-level scattering behavior in complex configurations, highlighting renewed interest in analytical and hybrid approaches for modern radar systems [3, 4, 6, 7]. However, most array-related studies still provide only general multi-object formulations [4, 5] or rely primarily on full-wave numerical simulations, without offering explicit closed-form RCS expressions for TCRAs. This motivates the need for an analytically tractable and general framework for predicting the RCS of modern metallic and dielectric TCRA configurations. In this work, the term *mosaic TCRA* refers to an array of trihedral corner reflectors arranged in a tightly packed triangular lattice, where adjacent reflectors may have different physical orientations. Unlike conventional uniform arrays composed of identical elements with identical orientations, mosaic TCRAs exhibit alternating orientations that influence the phase and amplitude contributions of individual reflectors at the array level. Unlike classical textbook formulations that focus primarily on isolated metallic trihedrals, recent studies have increasingly emphasized complex reflector architectures, reinforcing the need for analytical models that extend beyond traditional GO-based descriptions.

In addition to array-level limitations, the analytical modeling of individual TCR elements is also constrained. Most classical

* Corresponding author: Denys I. Zaikin (denys.zaikin@whitecellsystems.com).

models rely on geometrical-optical (GO) approximations, with the formulation of Groot [8] being the most widely referenced one. Although accurate for electrically large reflectors, these GO-based models do not directly extend to mosaic arrays that contain multiple reflector orientations or exhibit non-uniform phase behavior.

Research on dielectric corner reflectors, such as that presented in [9], has revealed additional material-dependent behaviors, particularly at millimeter-wave frequencies. However, these studies are limited to measurements in a single azimuthal plane and do not provide general analytical RCS expressions for dielectric TCRAs. Consequently, several aspects of TCRA behavior remain insufficiently understood, including the influence of alternating orientations in mosaic arrays, the interaction between GO-based models and full-wave phenomena for electrically small reflectors, and the highly non-symmetrical scattering characteristics observed in dielectric configurations. The core problem addressed in this study is the lack of a general, closed-form analytical model capable of predicting the monostatic RCS of metallic and dielectric TCRAs across arbitrary mosaic geometries and reflector sizes. In addition, the dielectric TCRA results obtained in this study are directly compared with the published measurement data from [9], providing experimental validation of the analytical and numerical models.

This study addresses these gaps by developing a unified analytical formulation for the monostatic RCS of trihedral corner reflector arrays, applicable to arbitrary mosaic geometries, reflector orientations, and a wide range of electrical sizes. The analytical developments were validated using full-wave simulations in COMSOL Multiphysics®, enabling a detailed comparison between GO-based closed-form predictions and wave-based numerical results for both metallic and dielectric TCRAs.

The main contributions of this work are summarized as follows:

- Development of a complete analytical framework for computing the monostatic RCS of TCRAs, covering multiple mosaic-array geometries, including arrays with dual-plane symmetry and irregular configurations.
- Derivation of a corrected and generalized complex-target RCS formulation based on multi-target scattering theory, resolving inconsistencies in existing array-factor approaches and incorporating the doubled propagation phase inherent to passive scattering.
- The inclusion of two distinct reflector orientations within the analytical model, enabled by a rigorous coordinate-system transformation, facilitates the accurate prediction of realistic mosaic layouts.
- Simplified closed-form approximations for the principal cuts ($\varphi = 0$ and $\varphi = \pi/2$) providing fast engineering tools for estimating grating-lobe angles, envelope widths, peak RCS, and scaling laws.
- Extensive full-wave validation performed using COMSOL, including comparison of four analytical single-reflector models, evaluation of multiple TCRA geometries from small to large arrays, and analysis of phase distortions and PML effects.
- Combined analytical and numerical investigations of dielectric TCRAs, revealing strong non-symmetry, orientation dependence, and reversed boresight offsets in the $\varphi = \pi/2$ plane (in comparison with metallic reflectors), as well as demonstrating that grating lobes remain predictable using the metal-array analytical model.
- Practical design guidelines for mosaic TCRAs, covering peak RCS scaling, angular characteristics, aperture-efficiency considerations, and the transition from corner reflectors to flat-plate behavior for electrically small reflectors.

The remainder of this manuscript is organized as follows. Section 2 introduces the definition of multi-target RCS. Section 3 extends the formulation to include two reflector orientations. Section 4 defines the mosaic TCRA geometry and coordinate system. Sections 5 and 6 present analytical models for single reflectors. Sections 7–9 derive closed-form expressions for arrays of various geometries. Section 10 provides full-wave validation, and Section 11 discusses the practical design implications.

2. MULTI-TARGET RADAR CROSS SECTION

The radar cross section of a single object is defined as follows [10]:

$$\sigma_0 = \lim_{R\to\infty} 4\pi R^2 \frac{|E_{RX}|^2}{|E_I|^2}, \tag{1}$$

where σ_0 is the RCS of a single target, R the distance from the radar to the target, E_{RX} the electric field strength at the radar receiver, and E_I the electric field strength incident at the target.

We now derive a general expression for the multi-target RCS σ. The multi-target configuration is shown in Fig. 1.

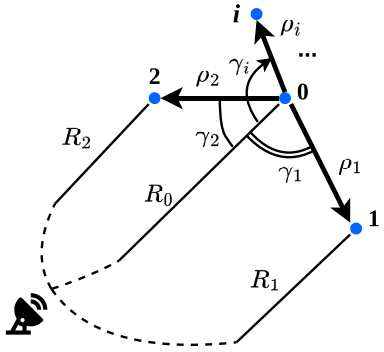

FIGURE 1. Setup for multi-target RCS derivation.

The electric field strength at the receiver from the ith target, E_{RXi}, can be expressed as:

$$\frac{E_{RXi}^2}{240\pi} = \frac{P_{TX}G_{TX}}{(4\pi R_i^2)^2}\sigma_i, \tag{2}$$

$$E_{RXi} = \frac{\sqrt{240\pi P_{TX}G_{TX}\sigma_i}}{4\pi R_i^2} e^{j(\omega_0 t - 2k_0 R_i)}, \tag{3}$$

where P_{TX} is the transmitted power, G_{TX} the transmitter antenna gain, $\omega_0 = 2\pi c/\lambda_0$ the carrier angular frequency, $k_0 =$

$2\pi/\lambda_0 = \omega_0/c$ the wave number, c the speed of light in free space, and $j = \sqrt{-1}$.

Assuming that the targets are located in the far-field region such that $R_0 \approx R_1 \approx R_2 \approx \cdots = R$, Eq. (3) is simplified to:

$$E_{RXi} = K\sqrt{\sigma_i}\, e^{j(\omega_0 t - 2k_0 R_i)}, \tag{4}$$

where K is a proportionality constant.

Further:

$$E_{RXi} = K\sqrt{\sigma_i}\, e^{j\omega_0 t} e^{j2k_0(R_0 - \rho_i \cos\gamma_i)}, \tag{5}$$

$$E_{RXi} = K\sqrt{\sigma_i}\, e^{j(\omega_0 t + 2k_0 R_0)} e^{-j2k_0 \rho_i \cos\gamma_i}. \tag{6}$$

Using (6), the total electric field at the receiver from N identical targets with RCS σ_0 is:

$$E_{RX} = K\sqrt{\sigma_0}\, e^{j(\omega_0 t + 2k_0 R_0)} \sum_{i=0}^{N-1} e^{-j2k_0 \rho_i \cos\gamma_i}, \tag{7}$$

$$E_{RX}^2 = K^2 \sigma_0 \left| \sum_{i=0}^{N-1} e^{-j2k_0 \rho_i \cos\gamma_i} \right|^2. \tag{8}$$

The incident electric field at the reference target ($i = 0$) is obtained from Fig. 1:

$$\frac{E_I^2}{240\pi} = \frac{P_{TX} G_{TX}}{4\pi R_i^2}, \tag{9}$$

$$E_I^2 = \frac{240\pi P_{TX} G_{TX}}{4\pi R_i^2} = 4\pi R^2 K^2. \tag{10}$$

Substituting (8) and (10) into (1), the expression for the complex target RCS becomes:

$$\sigma = \sigma_0 \left| \sum_{i=0}^{N-1} e^{-j2k_0 \rho_i \cos\gamma_i} \right|^2. \tag{11}$$

Equation (11) resembles the antenna array factor expression [11, Eq. (5.8)]:

$$AF = \sum_{i=0}^{N-1} A_i\, e^{j(\phi_i + k_0 \rho_i \cos\gamma_i)}, \tag{12}$$

where $A_i = I_i/I_0$ is the amplitude distribution, and ϕ_i is the phase distribution across the array elements.

Unlike active transmitting antennas, the complex target is modeled as a passive structure with uniform amplitude and phase distribution, that is, $A_i = 1$, $\phi_i = \text{const}$. Consequently, the summation term in (11) closely resembles the general antenna array factor in (12), with the following distinctions:

- Uniform amplitude and phase distribution: $A_i = 1$, $\phi_i = \text{const}$. This indicates that the target elements do not interact with each other, that is, no mutual coupling. The present work focuses on passive monostatic RCS evaluation; applications requiring precise phase control, such as phased-array beam steering or wavefront synthesis, are beyond the scope of this study.
- The phase term $-2k_0\rho_i \cos\gamma_i$ in (11) is twice that in (12) because of the round-trip propagation from the radar to the target and back.
- The phase term in (11) carries a negative sign compared to (12) because the RCS array factor is referenced to the radar location in Fig. 1.

The assumption of uniform amplitude and phase distribution ($A_i = 1$, $\phi_i = \text{const}$) implies negligible interaction between individual reflectors. This approximation is valid for electrically large trihedral corner reflectors and for arrays with moderate inter-element spacing, where single-bounce scattering dominates. For electrically small reflectors or extremely tightly packed arrays, mutual coupling, wave bypass, and phase distortion effects become increasingly significant. In such regimes, deviations from the analytical predictions are observed and are investigated using full-wave simulations in Section 10.

In conclusion, the antenna factor approach can be directly applied to analytically compute the RCS of a trihedral corner reflector array. For example, the planar array factor from [12, Eq. (6.88)] can be used by substituting the wave vector k with $-2k_0$. Thus, Eq. (11) can be finalized as:

$$\sigma = \sigma_0 |AF|^2, \tag{13}$$

where AF is the conventional antenna factor for linear or planar arrays [11, 12], with the following substitutions:

$$\begin{cases} A_i = 1, \\ \phi_i = \text{const}, \\ k \to -2k_0 \end{cases} \tag{14}$$

Equations (13) and (14) represent the corrected formulation for the complex target RCS and should replace [9, Eq. (7)].

The analytical formulation is intentionally based on geometrical-optics (GO) assumptions to preserve closed-form tractability. Wave-mechanical effects such as diffraction and coupling are not explicitly modeled and become significant for electrically small or tightly packed reflectors; these regimes are therefore investigated using full-wave simulations. Diffraction-aware extensions (e.g., PTD or UTD) are beyond the scope of this work.

3. MULTI-TARGET RADAR CROSS SECTION WITH INCLUSION OF TWO CORNER ORIENTATIONS

This section introduces the geometric orientations of the trihedral corner reflector elements and explains how these orientations influence the definition of the local coordinate systems. These conventions are required to derive the RCS of single reflectors and to construct array-level formulations.

An example of a mosaic TCRA is shown in Fig. 2. The array contains corner reflectors with two distinct orientations, as shown in Fig. 3. These orientations lead to different RCS expressions in the spherical coordinate system [13], as follows. Therefore, Eq. (13) cannot be applied directly.

The single-target RCS σ_0 must be replaced by two distinct cases: σ_1 for orientation 1 and σ_2 for orientation 2, as illustrated in Fig. 3. The original TCRA is partitioned into two sub-arrays:

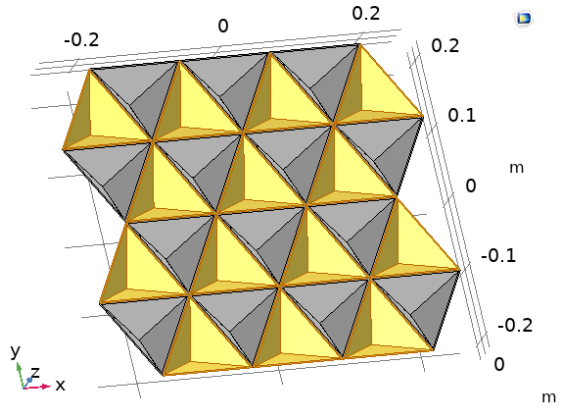

FIGURE 2. Example of a trihedral corner reflector array with Geometry 1: array with symmetry in two planes. TCRA divided into sub-arrays of reflectors with different orientations. An array with $N = 4$ rows and $M = 7$ columns is shown.

one consisting solely of reflectors with orientation 1 and the other with orientation 2, as illustrated in Fig. 2. Each sub-array has its own array factor, denoted AF_1 and AF_2, respectively.

Applying the superposition principle, Eqs. (7)–(8) are modified as follows:

$$E_{RX} = Ke^{j(\omega_0 t+2k_0R_0)}\left(\sqrt{\sigma_1}\sum_{i=0}^{N_1-1} e^{-j2k_0\rho_{1i}\cos\gamma_{1i}} + \sqrt{\sigma_2}\sum_{i=0}^{N_2-1} e^{-j2k_0\rho_{2i}\cos\gamma_{2i}}\right), \quad (15)$$

$$E_{RX} = Ke^{j(\omega_0 t+2k_0R_0)}\left(\sqrt{\sigma_1}AF_1 + \sqrt{\sigma_2}AF_2\right), \quad (16)$$

$$E_{RX}^2 = K^2\left|\sqrt{\sigma_1}AF_1 + \sqrt{\sigma_2}AF_2\right|^2. \quad (17)$$

Accordingly, Eq. (13) is updated as:

$$\sigma = \left|\sqrt{\sigma_1}AF_1 + \sqrt{\sigma_2}AF_2\right|^2, \quad (18)$$

which is consistent with the expressions in [4, Eq. (8)] and [5, Eq. (37)].

It is noted that, for the single-orientation case leading to (13), the sign of the phase term $-2k_0$ in (14) does not affect the monostatic RCS magnitude, since only the modulus of the array factor is evaluated. However, when multiple reflector orientations are combined at the field level, as in (18), the relative phase between the corresponding array-factor contributions must be retained, as it directly influences constructive and destructive interference effects. Consequently, the phase sign cannot be ignored in the general multi-orientation formulation.

4. MOSAIC ARRAY DEFINITION AND COORDINATE SYSTEM

This section defines the mosaic TCRA geometry and the coordinate system used throughout the analytical derivations.

A trihedral corner reflector array (TCRA) is shown in Fig. 2. Each individual reflector considered in this study was formed by three rectangular isosceles triangles. The reflector size is characterized by the cathetus length a, which can also be referred to as the reflector height, as shown in Fig. 3. In the array, reflectors with an aperture in the form of an equilateral triangle were placed tightly without gaps.

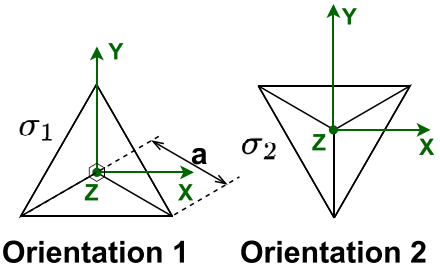

FIGURE 3. Two reflector orientations in the mosaic TCRA. Each trihedral corner reflector (TCR) consists of three rectangular isosceles triangles. The reflector size is defined by the cathetus length a.

The TCRA layout is defined by the number of rows N and columns M, as shown in Fig. 4, which represents an array with symmetry in two planes: $x = 0$ and $y = 0$. The array of size $N \times M$ in Fig. 4 is subject to the constraints $N = 2n$ and $M = 2m + 1$, where $n = 1, 2, \ldots$ and $m = 0, 1, 2, \ldots$ — that is, N must be an even integer, and M must be an odd integer. The minimum applicable TCRA size for this geometry is 2×1, based on the definition in Fig. 4. Fig. 4 also defines other geometric parameters and illustrates the division of the mosaic array into sub-arrays based on the reflector orientation. The array factor for such an array is derived in Section 7.

In the following sections, the geometry, in which the number of rows N is even, and the number of columns M is odd, is referred to as symmetry in two planes, as shown in Fig. 4, and is called Geometry 1. Specific configurations with 4- and 2-reflector arrays are discussed in Sections 8 and 9, respectively.

The spherical coordinate system used for the RCS calculations is shown in Fig. 5, where the z-axis represents the TCR boresight.

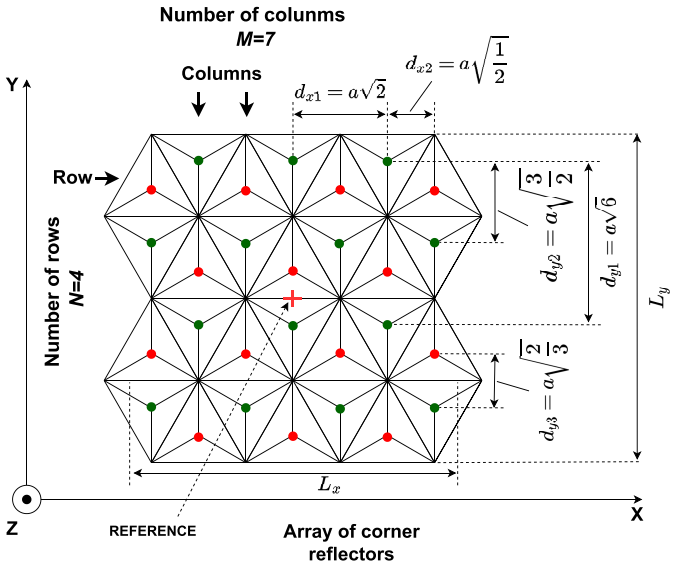

FIGURE 4. Geometry 1: array with symmetry in two planes ($x = 0$ and $y = 0$) and parameters of a TCRA composed of reflector groups. An example with $N = 4$ rows and $M = 7$ columns is shown.

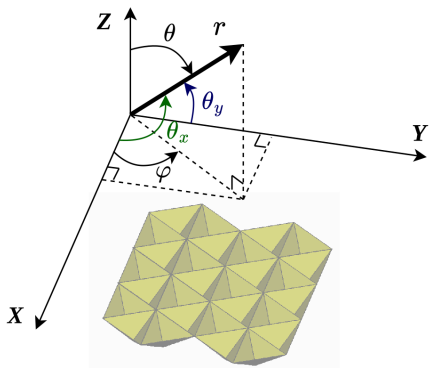

FIGURE 5. Coordinate system used for RCS derivation.

5. RADAR CROSS SECTION OF A SINGLE METAL REFLECTOR WITH ORIENTATION 1 AND 2

This section derives the monostatic RCS of a single metallic trihedral reflector by adapting the classical formulation of Groot to the coordinate system used in this study. The resulting expressions serve as building blocks for the array-level model presented later.

Models and analytical expressions for the RCS of a metal trihedral corner reflector can be found in several References [8, 13–16]. These studies are based on the geometrical optics method and assume the condition $a \gg \lambda_0$. Among them, [8, Eq. (4)] was selected in this study because it provides the most accurate analytical expression for the RCS. It should be noted that [15, Appendix A] appears to contain an error in the expression for ϕ', which, when corrected to $\phi' = \arctan(\sin\theta \sin\phi / \cos\theta)$, yields results consistent with [8, Eq. (4)].

To apply Groot's model in the coordinate system used throughout this work, a transformation is required between the "old" coordinate system defined in [8, Fig. 1] (also reproduced in Fig. 6) and the "new" coordinate system used in Figs. 3 and 5. Because the reflector orientation assumed in [8] does not coincide with the physical orientation of the reflectors inside the mosaic TCRA, the analytical expression must be evaluated at the angles (θ_1, φ_1) corresponding to the original system, while the incidence is described by (θ, φ) in the new system.

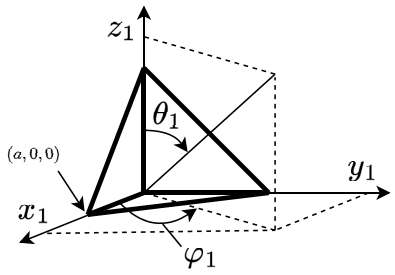

FIGURE 6. Original coordinate system used for RCS derivation in [8].

Accordingly, the expression for the RCS of a single reflector with orientation 1 is obtained using the approach in [8, Eq. (4)], together with the necessary coordinate transformation:

$$\sigma_1(\theta,\varphi) = 4\pi \frac{a^2}{\lambda_0} \times$$

$$\begin{cases} \frac{2\sin^2\theta_1 \sin(2\varphi_1)}{f(\theta_1,\varphi_1)}, & \begin{cases} \theta_1 < \operatorname{arccot}(\sqrt{2}\sin(\varphi_1+\frac{\pi}{4})) \cap \\ \theta_1 < \operatorname{arccot}(\sqrt{2}\cos(\varphi_1+\frac{\pi}{4})), \end{cases} \\ f(\theta_1,\varphi_1) - \frac{2}{f(\theta_1,\varphi_1)}, & \begin{cases} \theta_1 \geq \operatorname{arccot}(\sqrt{2}\sin(\varphi_1+\frac{\pi}{4})) \cap \\ \theta_1 < \operatorname{arccot}(\sqrt{2}\cos(\varphi_1+\frac{\pi}{4})), \end{cases} \\ \frac{2\sin(2\theta_1)\sin(\varphi_1)}{f(\theta_1,\varphi_1)}, & \begin{cases} \theta_1 > \operatorname{arccot}(\sqrt{2}\sin(\varphi_1+\frac{\pi}{4})) \cap \\ \theta_1 \geq \operatorname{arccot}(\sqrt{2}\cos(\varphi_1+\frac{\pi}{4})), \end{cases} \\ 0, & \begin{cases} \theta_1 < 0 \cap \\ \theta_1 > \frac{\pi}{2}, \end{cases} \\ 0, & \begin{cases} \varphi_1 < 0 \cap \\ \varphi_1 > \frac{\pi}{4}. \end{cases} \end{cases} \tag{19}$$

where

$$f(\theta_1,\varphi_1) = \sin\theta_1(\cos\varphi_1 + \sin\varphi_1) + \cos\theta_1. \tag{20}$$

The angular domain and symmetry conditions are enforced as follows:

$$\begin{cases} \theta_1(\theta,\varphi) = \arccos(z_1(\theta,\varphi)), \\ \varphi_1(\theta,\varphi) = \arcsin\left(\sin\left(\varphi_{1n}(\theta,\varphi) + \frac{\pi}{4}\right)\right) - \frac{\pi}{4}, \\ \varphi_{1n}(\theta,\varphi) = \operatorname{arctan2}(y_1(\theta,\varphi), x_1(\theta,\varphi)). \end{cases} \tag{21}$$

$$\begin{cases} x_1(\theta,\varphi) = -\frac{\sqrt{2}}{2}\sin\theta\cos\varphi - \frac{1}{\sqrt{6}}\sin\theta\sin\varphi + \frac{1}{\sqrt{3}}\cos\theta, \\ y_1(\theta,\varphi) = +\frac{\sqrt{2}}{2}\sin\theta\cos\varphi - \frac{1}{\sqrt{6}}\sin\theta\sin\varphi + \frac{1}{\sqrt{3}}\cos\theta, \\ z_1(\theta,\varphi) = +\frac{\sqrt{2}}{\sqrt{3}}\sin\theta\sin\varphi + \frac{1}{\sqrt{3}}\cos\theta. \end{cases} \tag{22}$$

Equation (19) is an optimized form of [8, Eq. (4)], where θ_1 and φ_1 are the angular coordinates defined in the original coordinate system. In contrast, θ and φ denote the angles in the new system used throughout this study. The expression for $\varphi_1(\theta,\varphi)$ in (21) enforces the domain constraints of the original model, which is valid only for $0 \leq \theta_1 \leq \pi/2$ and $0 \leq \varphi_1 \leq \pi/4$, and assumes symmetry about the plane $\varphi_1 = \pi/4$.

The transformation described in (22) is implemented using two passive coordinate rotations:

1. a rotation about the z-axis by $\alpha_1 = 3\pi/4$, and
2. a rotation about the x-axis by $\beta_1 = \arctan(\sqrt{2})$.

After these rotations, the new z-axis is aligned with the reflector boresight, consistent with the geometry shown in Figs. 4, 3, and 5.

$$R_z = \begin{bmatrix} \cos\alpha_1 & -\sin\alpha_1 & 0 \\ \sin\alpha_1 & \cos\alpha_1 & 0 \\ 0 & 0 & 1 \end{bmatrix},$$

$$R_x = \begin{bmatrix} 1 & 0 & 0 \\ 0 & \cos\beta_1 & -\sin\beta_1 \\ 0 & \sin\beta_1 & \cos\beta_1 \end{bmatrix}, \tag{23}$$

$$\begin{bmatrix} x_1(\theta,\varphi) \\ y_1(\theta,\varphi) \\ z_1(\theta,\varphi) \end{bmatrix} = R_z R_x \begin{bmatrix} \sin\theta\cos\varphi \\ \sin\theta\sin\varphi \\ \cos\theta \end{bmatrix}. \quad (24)$$

Here, (x_1, y_1, z_1) are the Cartesian coordinates of the unit vector in the original coordinate system, and (x, y, z) denote the corresponding coordinates in the new system. The rotation matrices in (24) represent a passive transformation of the coordinate axes [17, 14.10-6(c)], which is mathematically equivalent to an active rotation of the vector by inverse angles. Thus, if a function $g(\theta_1, \varphi_1)$ is defined in Groot's original system [8, Fig. 1], and we wish to evaluate it as $g(\theta, \varphi)$, the angle transformation proceeds as

$$(\theta,\varphi) \xrightarrow{(22)} \begin{bmatrix} x_1(\theta,\varphi) \\ y_1(\theta,\varphi) \\ z_1(\theta,\varphi) \end{bmatrix} \xrightarrow{(21)} (\theta_1,\varphi_1). \quad (25)$$

Finally, the RCS of a corner reflector with orientation 2 follows directly as:

$$\sigma_2(\theta,\varphi) = \sigma_1(\theta,\varphi-\pi). \quad (26)$$

6. COMPARISON OF RCS FOR ORIENTATIONS 1 AND 2

As shown in Fig. 7, only a minor difference in the RCS was observed between the two orientations in the yz-plane, whereas virtually no difference was observed in the xz-plane. This suggests that, in theory, the total RCS expression in (18) could be simplified back to the form of (13) under the assumption $\sigma_1(\theta,\varphi) = \sigma_2(\theta,\varphi)$, that is, the reflector orientation does not significantly affect the overall monostatic RCS. This observation is used in Section 11 to estimate the array characteristics.

Nevertheless, in this study, we retain the full expressions in Eqs. (18) and (34) for several reasons. The single-reflector RCS expressions (19) and (26), as well as the curves in Fig. 7, are based on the analytical model in [8, Eq. (4)]. Although accurate for electrically large trihedrals, this GO-based formulation does not fully capture the behavior of real TCRs, as demonstrated by the measurement data in [18, Fig. 14.8] and [15, Fig. 11]. The experimental RCS results clearly reveal asymmetry with respect to the elevation angle and the presence of "ears" caused by single-bounce, flat-plate reflections from individual faces, which are not represented in the analytical model.

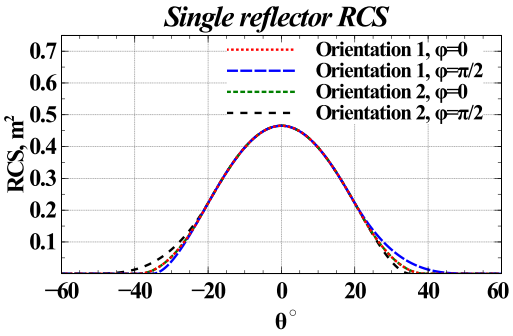

FIGURE 7. Comparison of RCS characteristics of single corner reflectors with orientations 1 and 2. Example parameters: $\lambda_0 = 0.03\,\text{m}$, $a = 0.1\,\text{m}$.

Furthermore, the effect of orientation was more pronounced for the dielectric reflectors. As demonstrated in Section 10.3, dielectric TCRs exhibit a highly non-symmetrical RCS pattern, particularly in the $\varphi = \pi/2$ plane, where internal reflections and refractions distort the characteristic shape. For these cases, retaining both orientations is essential for accurate array-level prediction.

In the future, more sophisticated individual-reflector models, such as those proposed in [19], may be incorporated. These models can capture additional wave interaction mechanisms at the cost of significantly increased computational complexity. In this case, the full expressions in (34), together with improved versions of (19) and (26), are required to obtain physically accurate TCRA predictions.

7. RADAR CROSS SECTION DERIVATION FOR ARRAY WITH SYMMETRY IN TWO PLANES (GEOMETRY 1)

This section derives the analytical RCS expression for Geometry 1 by combining the single-reflector model with the corresponding array-factor formulations for the two reflector orientations.

7.1. Array Factor for Reflectors with Orientation 1 in Geometry 1

The array factor for the group of reflectors with Orientation 1 in Geometry 1 (Fig. 4) is derived using the planar antenna array formulation introduced in Sections 2 and 3, as follows: The derivation follows the standard expressions in [12, Eq. (6.88)] and [10, Eq. (8.8)], together with the substitutions defined in Eq. (14). The resulting expression is as follows:

$$AF_1(\theta,\varphi) = \frac{\sin\left(\frac{M+1}{4}\Psi_{x1}\right)}{\sin\left(\frac{1}{2}\Psi_{x1}\right)} \cdot \frac{\sin\left(\frac{N}{4}\Psi_{y1}\right)}{\sin\left(\frac{1}{2}\Psi_{y1}\right)} \cdot e^{+j\frac{\Psi_{y3}}{2}} + \frac{\sin\left(\frac{M-1}{4}\Psi_{x1}\right)}{\sin\left(\frac{1}{2}\Psi_{x1}\right)} \cdot \frac{\sin\left(\frac{N}{4}\Psi_{y1}\right)}{\sin\left(\frac{1}{2}\Psi_{y1}\right)} \cdot e^{-j\Psi_{y3}}, \quad (27)$$

where the phase terms are defined as

$$\Psi_{x1} = -2k_0 d_{x1}\sin\theta\cos\varphi, \quad (28)$$

$$\Psi_{y1} = -2k_0 d_{y1}\sin\theta\sin\varphi, \quad (29)$$

$$\Psi_{y3} = -2k_0 d_{y3}\sin\theta\sin\varphi, \quad (30)$$

and the geometric spacings are $d_{x1} = a\sqrt{2}$, $d_{y1} = a\sqrt{6}$, and $d_{y3} = a\sqrt{2/3}$, as shown in Fig. 4.

These phase expressions follow directly from the scalar-product relationship presented earlier in (11)–(12), where

$$\rho_i\cos\gamma_i = \rho_i\frac{\vec{\rho_i}\cdot\vec{R_0}}{\rho_i R_0}. \quad (31)$$

This reduces to

$$\rho_i\cos\gamma_i = \frac{\vec{\rho_i}\cdot\vec{R_0}}{R_0} = dx_i\sin\theta\cos\varphi + dy_i\sin\theta\sin\varphi$$

$$+dz_i \cos\theta, \tag{32}$$

where (dx_i, dy_i, dz_i) are the Cartesian components of $\vec{\rho}_i$ defined with respect to the origin in Fig. 1.

7.2. Array Factor for Reflectors with Orientation 2 in Geometry 1

The array factor for reflectors with Orientation 2 in Geometry 1 is derived in a similar manner using the planar array formulation of [12] and [10], together with the substitutions from Eq. (14). The resulting expression is as follows:

$$AF_2(\theta,\varphi) = \frac{\sin\left(\frac{M+1}{4}\Psi_{x1}\right)}{\sin\left(\frac{1}{2}\Psi_{x1}\right)} \cdot \frac{\sin\left(\frac{N}{4}\Psi_{y1}\right)}{\sin\left(\frac{1}{2}\Psi_{y1}\right)} \cdot e^{-j\frac{\Psi_{y3}}{2}} + \frac{\sin\left(\frac{M-1}{4}\Psi_{x1}\right)}{\sin\left(\frac{1}{2}\Psi_{x1}\right)} \cdot \frac{\sin\left(\frac{N}{4}\Psi_{y1}\right)}{\sin\left(\frac{1}{2}\Psi_{y1}\right)} \cdot e^{+j\Psi_{y3}}, \tag{33}$$

with identical definitions of Ψ_{x1}, Ψ_{y1}, and Ψ_{y3} given by (28)–(30). The geometric offsets are $d_{x1} = a\sqrt{2}$, $d_{y1} = a\sqrt{6}$, $d_{x2} = a/\sqrt{2}$, $d_{y2} = a\sqrt{3/2}$, and $d_{y3} = a\sqrt{2/3}$. These values must be modified if additional spacing is introduced between the reflectors.

Equations (27) and (33) apply to any array of size $N \times M$ subject to $N = 2n$ and $M = 2m + 1$ ($n \geq 1$, $m \geq 0$), that is, arrays with symmetry in both the xz- and yz-planes. The smallest valid array size for this geometry was 2×1. Further examples, including 4-reflector and $1 \times M$ arrays, are discussed in Sections 8 and 9. These expressions can also be compared with the formulation in [20, Eq. (5)].

7.3. Final Expression for an $N \times M$ Array in Geometry 1

Using the single-reflector RCS model and derived array factors, this section presents the final closed-form expression for the monostatic RCS of a general $N \times M$ TCRA. This expression forms the analytical core of the proposed framework.

Using the combined contribution of both orientations, the monostatic RCS of the TCRA is

$$\sigma(\theta,\varphi) = \left|\sqrt{\sigma_1(\theta,\varphi)}\,AF_1(\theta,\varphi) + \sqrt{\sigma_2(\theta,\varphi)}\,AF_2(\theta,\varphi)\right|^2, \tag{34}$$

where $\sigma_1(\theta,\varphi)$ and $\sigma_2(\theta,\varphi)$ are given by Eqs. (19) and (26), respectively. This expression applies to any array with an even N and an odd M.

7.4. Approximation for $\varphi = 0$ Plane

As shown in Fig. 7, the RCS of the individual reflectors with orientations 1 and 2 are nearly identical for $\varphi = 0$. Thus, $\sigma_1 \approx \sigma_2$, and Eq. (13) may be used. Under this assumption, Eqs. (27) and (33) simplify to

$$AF_1(\theta,0) = AF_2(\theta,0) = \frac{N}{2} \cdot \frac{\sin\left(\frac{M+1}{4}\Psi_{x1}\right)}{\sin\left(\frac{1}{2}\Psi_{x1}\right)} + \frac{N}{2} \cdot \frac{\sin\left(\frac{M-1}{4}\Psi_{x1}\right)}{\sin\left(\frac{1}{2}\Psi_{x1}\right)}, \tag{35}$$

leading to the total factor

$$AF(\theta,0)\big|_{\sigma_1=\sigma_2} = AF_1(\theta,0) + AF_2(\theta,0). \tag{36}$$

This becomes

$$AF(\theta,0) = 2N \cdot \frac{\sin\left(\frac{M+1}{4}\Psi_{x1}\right) + \sin\left(\frac{M-1}{4}\Psi_{x1}\right)}{\sin\left(\frac{1}{2}\Psi_{x1}\right)}, \tag{37}$$

and simplified further to

$$AF(\theta,0) = N \cdot \frac{\sin\left(\frac{M}{4}\Psi_{x1}\right)}{\sin\left(\frac{1}{4}\Psi_{x1}\right)}. \tag{38}$$

Substituting into (13) yields

$$\sigma(\theta,0) = \sigma_1(\theta,0) \cdot \left| N \frac{\sin\left(\frac{M}{4}\Psi_{x1}\right)}{\sin\left(\frac{1}{4}\Psi_{x1}\right)} \right|^2, \tag{39}$$

with $\Psi_{x1} = -2k_0 d_{x1} \sin\theta$.

7.5. Approximation for $\varphi = \pi/2$ Plane

A similar simplification can be performed for the $\varphi = \pi/2$ plane. Applying the same assumptions as above leads to

$$AF_1\left(\theta,\frac{\pi}{2}\right) = \frac{M+1}{2}\frac{\sin\left(\frac{N}{4}\Psi_{y1}\right)}{\sin\left(\frac{1}{2}\Psi_{y1}\right)} e^{+j\frac{\Psi_{y3}}{2}} + \frac{M-1}{2}\frac{\sin\left(\frac{N}{4}\Psi_{y1}\right)}{\sin\left(\frac{1}{2}\Psi_{y1}\right)} e^{-j\Psi_{y3}}, \tag{40}$$

$$AF_2\left(\theta,\frac{\pi}{2}\right) = \frac{M+1}{2}\frac{\sin\left(\frac{N}{4}\Psi_{y1}\right)}{\sin\left(\frac{1}{2}\Psi_{y1}\right)} e^{-j\frac{\Psi_{y3}}{2}} + \frac{M-1}{2}\frac{\sin\left(\frac{N}{4}\Psi_{y1}\right)}{\sin\left(\frac{1}{2}\Psi_{y1}\right)} e^{+j\Psi_{y3}}, \tag{41}$$

and the combination gives

$$AF\left(\theta,\frac{\pi}{2}\right) = \frac{\sin\left(\frac{N}{4}\Psi_{y1}\right)}{\sin\left(\frac{1}{2}\Psi_{y1}\right)}\left((M+1)\cos\frac{\Psi_{y3}}{2} + (M-1)\cos\Psi_{y3}\right). \tag{42}$$

For $M \gg 1$, this becomes

$$AF\left(\theta,\frac{\pi}{2}\right) \approx M\,\frac{\sin\left(\frac{N}{4}\Psi_{y1}\right)}{\sin\left(\frac{1}{2}\Psi_{y1}\right)}\left(\cos\frac{\Psi_{y3}}{2} + \cos\Psi_{y3}\right). \tag{43}$$

Since $d_{y1} = 3d_{y3}$ and $\Psi_{y1} = 3\Psi_{y3}$, the result is simplified to

$$AF\left(\theta,\frac{\pi}{2}\right) \approx M\frac{\sin\left(\frac{N}{4}\Psi_{y1}\right)}{\sin\left(\frac{1}{4}\Psi_{y1}\right)}\cos\left(\frac{\Psi_{y1}}{12}\right). \tag{44}$$

Substituting into (13) yields

$$\sigma\left(\theta,\frac{\pi}{2}\right) \approx \frac{\sigma_1\left(\theta,\frac{\pi}{2}\right) + \sigma_2\left(\theta,\frac{\pi}{2}\right)}{2}$$

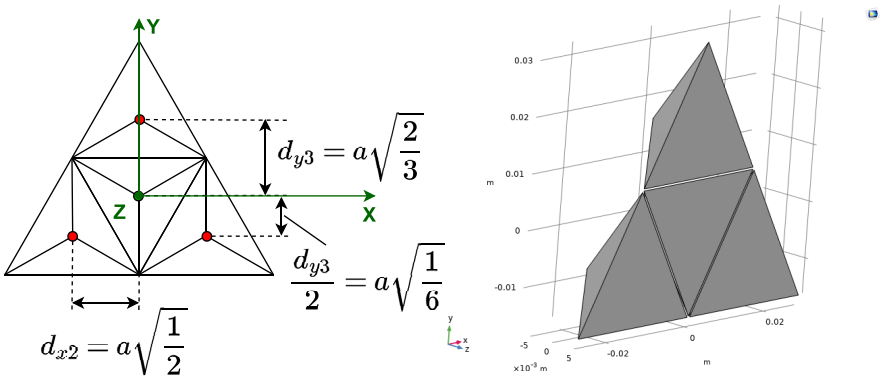

FIGURE 8. TCRA geometry reproduced from [9, Fig. 7].

$$\cdot \left| M \frac{\sin\left(\frac{N}{4}\Psi_{y1}\right)}{\sin\left(\frac{1}{4}\Psi_{y1}\right)} \cos\left(\frac{\Psi_{y1}}{12}\right) \right|^2, \quad (45)$$

with $\Psi_{y1} = -2k_0 d_{y1} \sin\theta$.

Finally, note that the cosine term modulates the main-lobe envelope, attenuating two-thirds of the lobes and widening the angular spacing by a factor of three. This effect reappears in Sections 11 and 10.2, respectively.

8. RADAR CROSS SECTION FOR ARRAY OF FOUR REFLECTORS WITH GEOMETRY FROM [9]

In this section, the general RCS framework is applied to the special case of a four-reflector array, corresponding to the geometry reported in [9].

Using the approach described in Sections 2 and 3, the analytical expression for the RCS of a metal TCRA with the configuration shown in [9, Fig. 7] (reproduced in Fig. 8) is given by:

$$\sigma_{4R}(\theta,\varphi) = \left| \sqrt{\sigma_1(\theta,\varphi)} \left(e^{j\Psi_{y3}} + 2\cos(\Psi_{x2})\, e^{-j\frac{\Psi_{y3}}{2}} \right) + \sqrt{\sigma_2(\theta,\varphi)} \right|^2, \quad (46)$$

where:

$$\Psi_{x2} = -2k_0 d_{x2} \sin\theta\cos\varphi, \quad (47)$$
$$\Psi_{y3} = -2k_0 d_{y3} \sin\theta\sin\varphi, \quad (48)$$

with $d_{x2} = a/\sqrt{2}$ and $d_{y3} = a\sqrt{2/3}$, as defined in Fig. 4. In addition:

- $\sigma_1(\theta,\varphi)$ is defined by Eq. (19),
- $\sigma_2(\theta,\varphi)$ is defined by Eq. (26).

9. RADAR CROSS SECTION FOR $1 \times M$ ARRAY OF REFLECTORS

In this section, the RCS expression for a $1 \times M$ linear array of TCRs is derived, resulting in simplified closed-form formulas for this geometry.

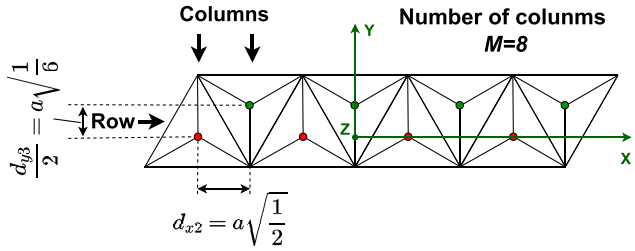

FIGURE 9. Geometry of the $1 \times M$ array.

For the $1 \times M$ array of metal trihedral corner reflectors (TCRA), illustrated in Fig. 9, the radar cross section (RCS) can be derived as:

$$\sigma_{1\times M}(\theta,\varphi) = \left(\frac{\sin\left(\frac{M}{4}\Psi_{x1}\right)}{\sin\left(\frac{1}{2}\Psi_{x1}\right)} \right)^2 \cdot \left| \sqrt{\sigma_1(\theta,\varphi)} + \sqrt{\sigma_2(\theta,\varphi)}\, e^{j\left(\Psi_{x2}+\frac{\Psi_{y3}}{2}\right)} \right|^2, \quad (49)$$

where

$$\Psi_{x1} = -2k_0 d_{x1} \sin\theta\cos\varphi, \quad (50)$$
$$\Psi_{x2} = -2k_0 d_{x2} \sin\theta\cos\varphi, \quad (51)$$
$$\Psi_{y3} = -2k_0 d_{y3} \sin\theta\sin\varphi, \quad (52)$$

with $d_{x1} = a\sqrt{2}$, $d_{x2} = a/\sqrt{2}$, and $d_{y3} = a\sqrt{2/3}$, as defined in Fig. 4. The array size is constrained by $M = 2m$, where $m = 1, 2, \ldots$, meaning that M must be an even integer.

As a specific example, for a two-reflector configuration in a 1×2 array ($M = 2$), Eq. (49) is simplified to:

$$\sigma_{1\times 2}(\theta,\varphi) = \left| \sqrt{\sigma_1(\theta,\varphi)} + \sqrt{\sigma_2(\theta,\varphi)}\, e^{j\left(\Psi_{x2}+\frac{\Psi_{y3}}{2}\right)} \right|^2. \quad (53)$$

10. COMSOL SIMULATION

This section validates the analytical model using full-wave FEM simulations in COMSOL Multiphysics. Simulations were performed for single reflectors, metallic arrays, and dielectric

arrays to assess the model accuracy across a wide range of reflector sizes and materials.

The presented results are consistent with recent analytical and numerical studies addressing both high-frequency corner reflector behavior and array-level scattering mechanisms in modern radar systems [6, 7].

10.1. Single Metal Corner Reflector Simulation

This subsection evaluates the accuracy of the analytical single-reflector RCS expressions by comparing them with the full-wave simulations of isolated TCRs. The goal was to quantify the validity range of the GO theory and identify wave-based effects that are not captured by closed-form models.

We first compare the analytical expressions for a single TCR from (19) — based on [8, Eq. (4)] and its correction in [15, Appendix A] — together with [13, Eq. (23)], [16, p. 241], and [14], against full-wave FEM simulations in COMSOL Multiphysics [21]. The TCR with Orientation 1 is positioned as shown in Figs. 3 and 5, with its boresight aligned to the z-axis. A vertically polarized incident plane wave illuminates the reflector along the r-axis, fixing $\varphi = \pi/2$, while θ is scanned, as shown in Fig. 10.

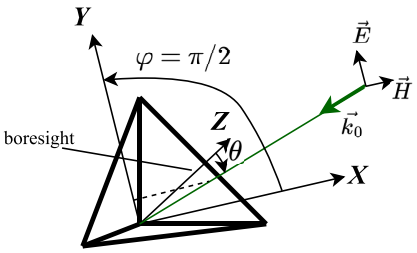

FIGURE 10. Setup for the monostatic RCS simulation of the single TCR $\varphi = \pi/2$.

The COMSOL simulations used a linearly polarized plane wave, and the monostatic RCS was obtained from the *total* scattered electric field, without co-/cross-polar decomposition. While ideal PEC trihedrals produce negligible cross-polarization under GO assumptions [6], practical factors, such as finite edge thickness, non-ideal geometry, and internal reflections, can generate small cross-polar terms. These are naturally included in the total-field FEM results and may contribute to small discrepancies relative to the analytical, purely co-polar GO models.

For $\varphi = \pi/2$, symmetry about the $x = 0$ plane allows simulating only half of the geometry, thereby reducing the computational cost. The wavelength is fixed at $\lambda_0 = 0.03\,\text{m}$, and the TCR height is varied as follows:

$$a = \{0.01,\ 0.03,\ 0.1,\ 0.2,\ 0.3\}\,\text{m},$$

to analyze the influence of the electrical size. The simulated and analytical results are shown in Fig. 11.

Analyzing Fig. 11, several trends can be identified:

- **Large reflectors ($a \gg \lambda_0$):** Analytical models match FEM results closely (e.g., $a = 0.3\,\text{m}$), confirming GO accuracy in the electrically large regime.
- **Moderate electrical size ($a \sim 3\lambda_0$):** For $a = 0.1\,\text{m}$, edge diffraction begins to alter the pattern near the boresight, producing features absent in GO-only models.
- **Asymmetry and "ears":** The analytical model in [8] predicts mild asymmetry in the $\varphi = \pi/2$ plane, which appears in both theory and simulation. The FEM also reveals "ears" caused by single-bounce flat-plate reflections [18, Fig. 14.8], which cannot be captured by simple analytical models.
- **Near-resonant case ($a \approx \lambda_0$):** For $a = 0.03\,\text{m}$, resonance-like behavior and shifted maxima are observed, similar to the Mie-type effects [18, 22]. The GO models still predict the peak magnitude reasonably well but not the angular placement.
- **Small reflectors ($a \ll \lambda_0$):** For $a = 0.01\,\text{m}$, RCS values exceed the GO estimate $\sigma_{\text{GO}}^{\text{peak}} = 4\pi a^4/(3\lambda^2)$ [15]. The RCS becomes nearly omnidirectional, indicating that small TCRs remain effective scatterers even though aperture-based models are no longer applicable.
- **Implications for arrays:** When used in a TCRA, electrically small TCRs do not follow the free-space single-element RCS because of mutual interaction, shadowing, and wave bypass. In such cases, direct AF multiplication in (34) may not yield accurate array-level predictions.
- **Wall thickness:** The reflector-wall thickness (set to $t = 1.5 \times 10^{-3}\,\text{m}$ for $a \geq 0.1\,\text{m}$ and $t = 1.5 \times 10^{-4}\,\text{m}$ for $a < 0.1\,\text{m}$) has a minor but noticeable effect on the RCS.

10.2. Metal Corner Reflectors Array Simulation

This subsection compares the analytical array model with FEM simulations for metallic mosaic arrays of increasing sizes. The results highlighted the impact of the electrical size of the reflector, array aperture, and numerical settings on model accuracy.

In this section, the analytical predictions from (34) are compared with the full-wave FEM simulations performed in COMSOL Multiphysics [21]. The TCRA is positioned as shown in Fig. 5, with each reflector's boresight aligned along the z-axis. A vertically polarized plane wave illuminates the array along the r-axis, and the monostatic RCS is obtained by sweeping the elevation angle θ for the two principal planes, $\varphi = 0$ and $\varphi = \pi/2$.

Geometry 1 (Fig. 4) exhibits symmetry in both the xz- and yz-planes, enabling the simulation of only half of the structure for both principal cuts. This significantly reduces computational cost compared with the single-reflector case, where symmetry applies only for $\varphi = \pi/2$. To simulate $\varphi = 0$, the geometry is simply rotated by 90° around the z-axis while keeping $\varphi = \pi/2$ fixed, avoiding remeshing for each azimuth.

Two Perfectly Matched Layer (PML) shapes were used in the selected simulations. Rectangular PMLs require fewer resources but may underestimate the main-lobe amplitude, whereas spherical PMLs provide better accuracy at the cost of occasional artifacts and additional side lobes. For electrically larger reflectors ($a \geq 0.1\,\text{m}$), a coarser mesh (one-half to one-third of λ_0) was used to manage memory usage, with a minor impact on accuracy. All simulation files are available as open-source datasets (Section 13).

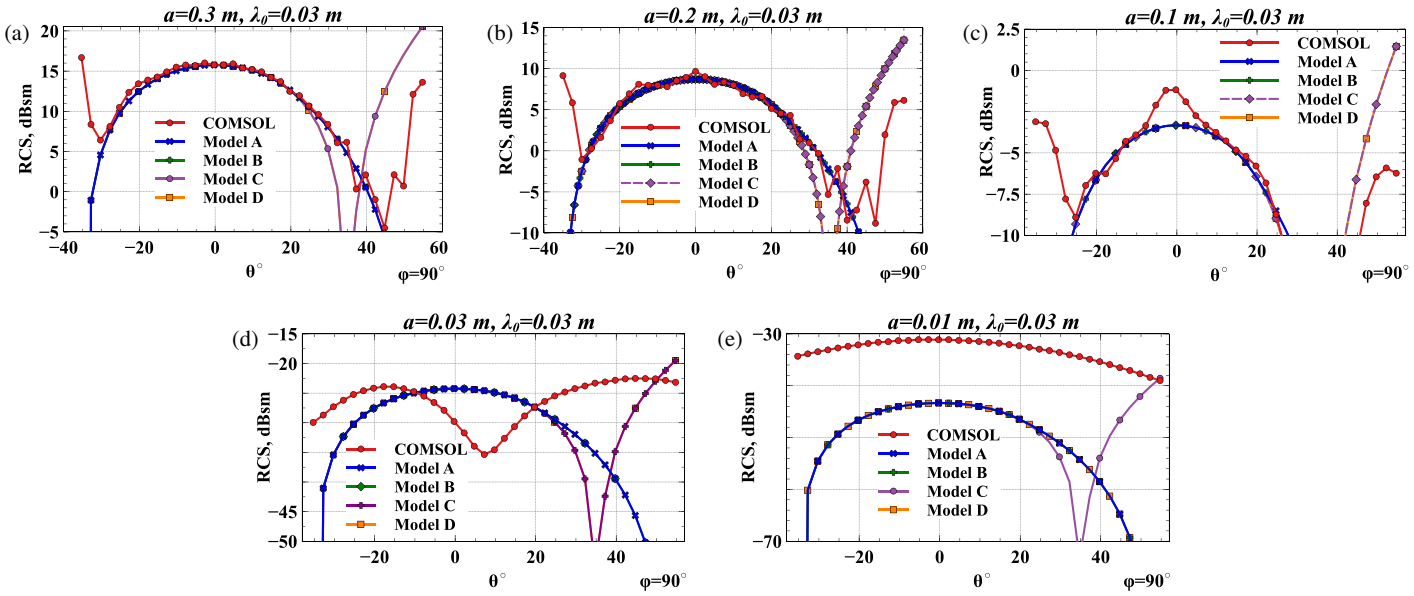

FIGURE 11. COMSOL simulation of a single trihedral corner reflector for $\lambda_0 = 0.03\,\text{m}$ and $\varphi = 90°$. Model A: Eq. (19) [8, Eq. (4)]; Model B: corrected [15, Appendix A]; Model C: [13, Eq. (23)]; Model D: [14]. (a) $a = 0.3\,\text{m}$, (b) $a = 0.2\,\text{m}$, (c) $a = 0.1\,\text{m}$, (d) $a = 0.03\,\text{m}$, (e) $a = 0.01\,\text{m}$.

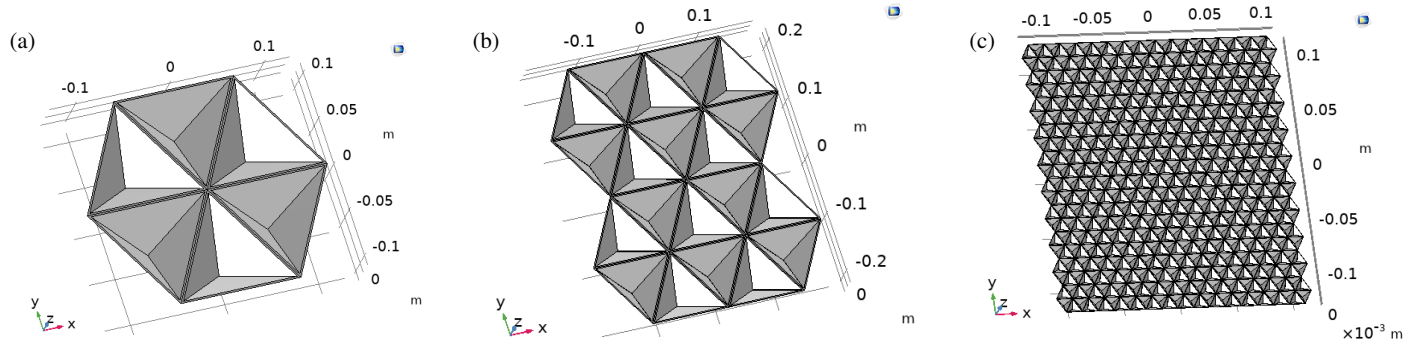

FIGURE 12. COMSOL simulation setup for the monostatic RCS of the TCRA for Geometry 1. (a) $N = 2$, $M = 3$; (b) $N = 4$, $M = 5$; (c) $N = 20$, $M = 31$.

As summarized in Section 4, Geometry 1 corresponds to arrays with an even number of rows ($N = 2n$) and an odd number of columns ($M = 2m + 1$), guaranteeing symmetry in two orthogonal planes.

10.2.1. $N = 2$, $M = 3$ (Geometry 1)

The simulation geometry for this case is shown in Fig. 12(a). Comparisons between the analytical predictions and FEM results for several reflector sizes are shown in Fig. 13. The results demonstrate the expected dependence on electrical size: good agreement when $a \geq \lambda_0$, increasing deviations when $a \approx \lambda_0$ owing to diffraction and coupling effects, and flat-plate-like behavior when $a \ll \lambda_0$.

10.2.2. $N = 4$, $M = 5$ (Geometry 1)

The $N = 4$, $M = 5$ configuration is shown in Fig. 12(b), with an example comparison in Fig. 14(a). Increasing the number of elements enhances the overall RCS but also amplifies the contribution of wave-based effects when a is only a few wavelengths.

10.2.3. $N = 20$, $M = 31$ (Geometry 1)

The large-array configuration ($N = 20$, $M = 31$) is shown in Fig. 12(c). A representative comparison for $a = 0.01\,\text{m}$ is shown in Fig. 14(b). When $a \ll \lambda_0$, but the array aperture is electrically large, the overall RCS approaches that of a flat metallic plate with dimensions $L_x \times L_y$.

Analyzing Figs. 13 and 14, the following observations can be made:

- Equation (34) agrees well with the FEM simulations for reflector heights $a \geq \lambda_0$, where the GO assumptions hold, and array-factor multiplication remains valid.
- For $a \ll \lambda_0$, the aggregate behavior approaches that of a metallic plate of size $L_x \times L_y$, as expected when the individual reflectors are electrically small, and the aperture dominates the scattering.

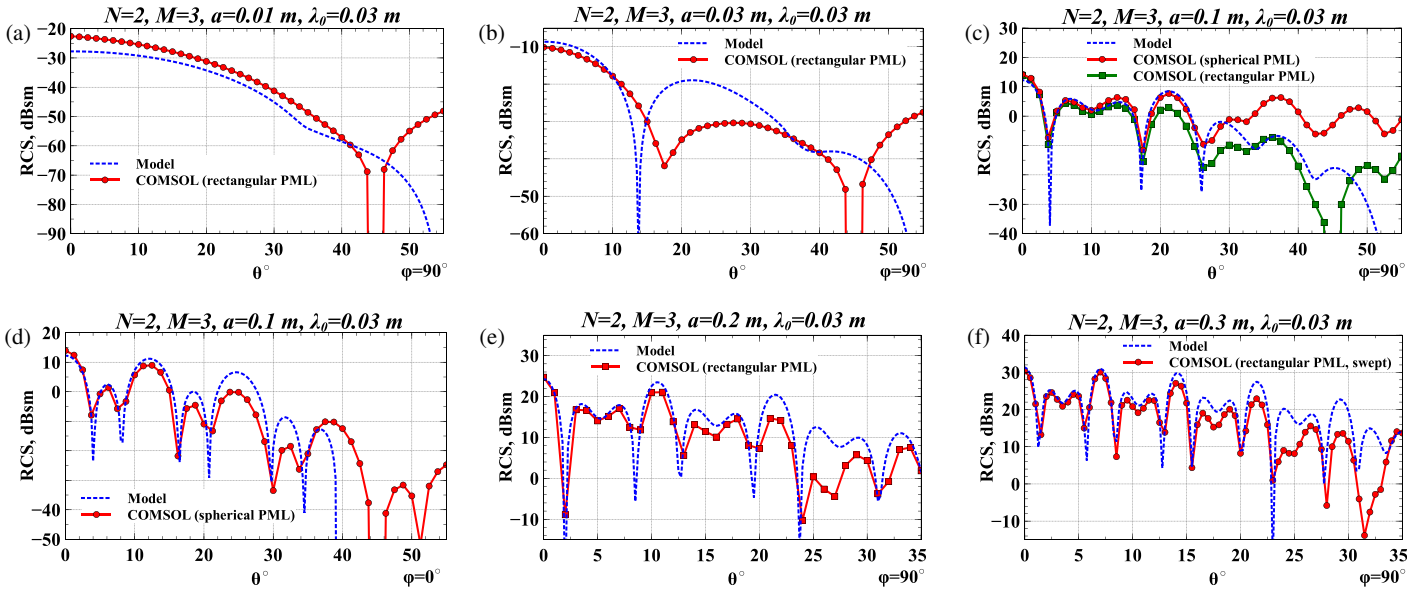

FIGURE 13. COMSOL simulation of the corner reflector array for $N = 2$, $M = 3$ and $\lambda_0 = 0.03\,\text{m}$. Analytical model: Eq. (34). (a) $a = 0.01\,\text{m}$, $\varphi = 90°$; (b) $a = 0.03\,\text{m}$, $\varphi = 90°$; (c) $a = 0.1\,\text{m}$, $\varphi = 90°$; (d) $a = 0.1\,\text{m}$, $\varphi = 0°$; (e) $a = 0.2\,\text{m}$, $\varphi = 90°$; (f) $a = 0.3\,\text{m}$, $\varphi = 90°$.

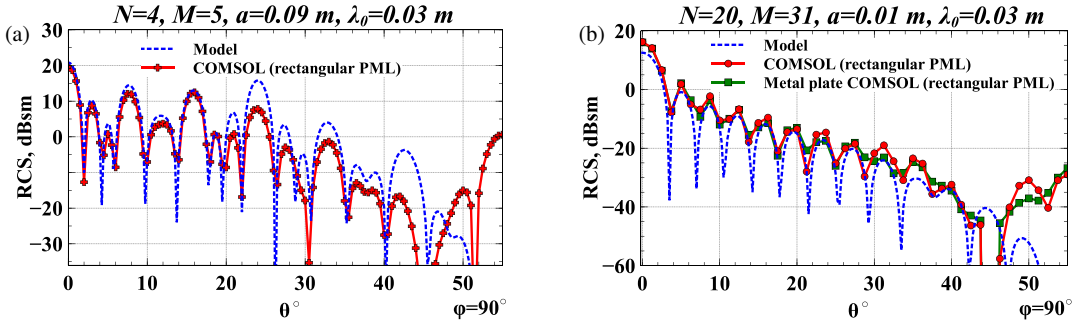

FIGURE 14. COMSOL simulation of the corner reflector array for $\lambda_0 = 0.03\,\text{m}$, $\varphi = 90°$. Analytical model — Eq. (34). (a) $N = 4$, $M = 5$, $a = 0.09\,\text{m}$; (b) $N = 20$, $M = 31$, $a = 0.01\,\text{m}$.

- PML geometry affects numerical accuracy: rectangular PMLs are efficient but may underestimate the main-lobe RCS, whereas spherical PMLs provide higher fidelity at the cost of occasional artifacts and increased memory use.

Finally, geometrical-optics-based derivations assume equal optical path lengths for all the reflected rays [8]. For a limited a/λ_0, edge diffraction and corner resonances violate this assumption. Therefore, a dedicated phase-scan simulation was performed for incidence at $\theta = \pm 10°$ (setup shown in Fig. 15). The measured phase differences in Fig. 16 confirm that the phase distortions increase as a/λ_0 decreases, thereby altering the effective array factor. These effects must be considered when analyzing or designing TCRAs that comprise electrically small reflectors.

10.3. Dielectric Array of Four Reflectors with Geometry from [9]

This subsection extends the analysis to dielectric reflectors by comparing analytical predictions with FEM simulations and published measurement data. The goal was to examine how dielectric loading and internal reflections modified the array behavior.

The present study primarily focuses on the modeling and simulation of metallic TCRAs. However, [9] reports measurements of a four-element array of dielectric trihedral reflectors arranged in the geometry shown in Fig. 8. In [9, Fig. 7], only the $\varphi = 0$ plane was measured experimentally. In this section, we extended the analysis by simulating both principal planes, $\varphi = 0$ and $\varphi = \pi/2$, using COMSOL Multiphysics, and compared the results with the analytical expression (46).

The simulation parameters are chosen to match those reported in [9] as closely as computationally feasible. Two reflector sizes were considered: $a = 0.041\,\text{m}$, corresponding to the original geometry, and a reduced size of $a = 0.02\,\text{m}$. A smaller size was employed to limit the computational cost and memory requirements while maintaining sufficient accuracy. For the larger reflector, the mesh size was approximately $\lambda_0/1.3$, whereas for the smaller reflector, it was approximately $\lambda_0/2$, ensuring reasonable convergence.

The frequency was fixed at 76.5 GHz, corresponding to a wavelength of $\lambda_0 = 3.92 \times 10^{-3}\,\text{m}$. The dielectric material

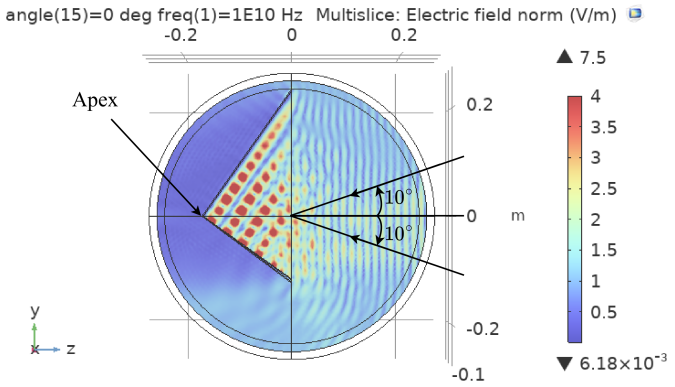

FIGURE 15. COMSOL simulation setup for phase measurement of the reflected wave at a far-field reference point ($R = 1\,\text{m}$). $\lambda_0 = 0.03\,\text{m}$, $\varphi = 90°$.

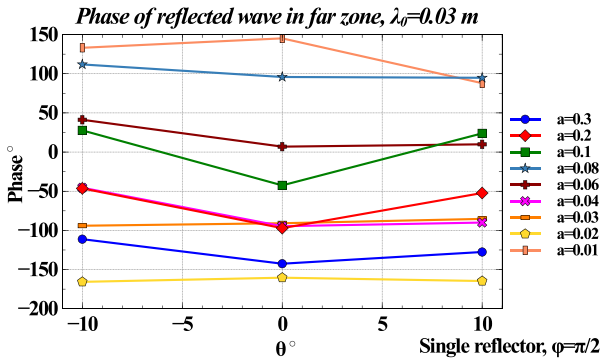

FIGURE 16. Results of COMSOL simulation of phase measurement of the reflected wave at a far-field reference point ($R = 1\,\text{m}$). $\lambda_0 = 0.03\,\text{m}$, $\varphi = 90°$.

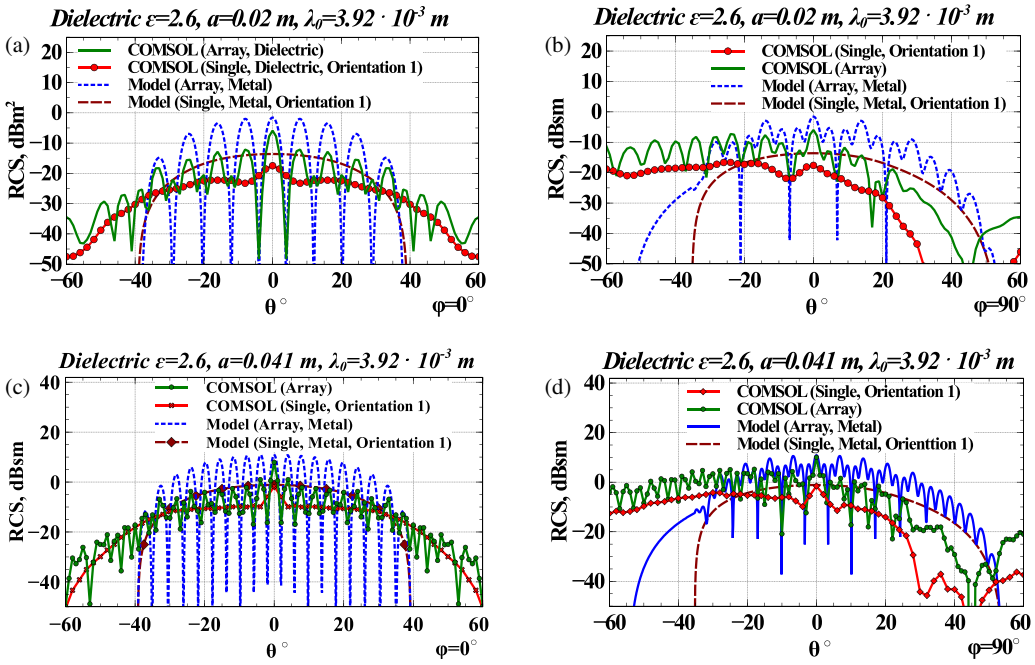

FIGURE 17. COMSOL simulation of the dielectric corner reflector array of four reflectors with geometry from [9]. Dielectric material parameters: $\varepsilon = 2.6$, $\tan\delta = 0.001$, $\lambda_0 = 3.92 \cdot 10^{-3}$ m. Analytical model — Eq. (46). (a) $a = 0.02\,\text{m}$, $\varphi = 0°$; (b) $a = 0.02\,\text{m}$, $\varphi = 90°$; (c) $a = 0.041\,\text{m}$, $\varphi = 0°$; (d) $a = 0.041\,\text{m}$, $\varphi = 90°$.

used in the simulations has a relative permittivity of $\varepsilon_r = 2.6$ and a loss tangent of $\tan\delta = 0.001$, consistent with polystyrene as reported in [9]. The simulated and analytical results are presented in Fig. 17.

Analyzing Fig. 17, the following observations can be made:

- For $\varphi = 0$, the simulation results agree well with the experimental data reported in [9, Fig. 7]. This validated both the simulation setup and analytical model for this plane.
- For $\varphi = \pi/2$ (Figs. 17(b) and (d)), the scattering characteristics become highly non-symmetrical. Both the single dielectric TCR and the four-element array exhibit nearly constant RCS levels over a wide range of θ, and the main lobe of the single dielectric TCR is shifted in the opposite direction compared with the metal case. This inversion of the offset propagates to the array response and is consistent with multiple internal reflections and refractions within the dielectric structure.
- Despite these differences, the grating-lobe positions predicted by Eq. (46) remain accurate. This confirms that the array-factor-based formulation captures the dominant angular periodicity even for dielectric TCRAs.
- The RCS values for both the TCR and TCRA exhibited a clear peak near the boresight direction. This peak likely arises from enhanced constructive reflections along that direction, whereas at oblique angles, a larger fraction of the energy escapes owing to dielectric transmission and surface scattering.

- The peak RCS of the dielectric TCRA is approximately 0–5 dB lower than that of an equivalent metal TCRA. This reduction may be attributed to the dielectric losses, reduced reflection coefficients at the dielectric-air interface, and internal energy absorption. Further studies are required to quantify these effects.

The peak-RCS overestimation in Fig. 17 arises from applying a metal-array geometrical-optics model to dielectric TCRAs. In dielectric structures, transmission, internal refraction, and element-dependent phase distortions reduce coherent backscattering relative to ideal GO predictions. Consequently, dielectric TCRA behavior is primarily investigated using full-wave FEM simulations, while the analytical formulation continues to accurately predict grating-lobe locations and the dominant angular periodicity.

11. CHARACTERISTICS OF A GENERIC METAL MOSAIC TCRA

This section summarizes the key analytical characteristics of electrically large mosaic arrays using the closed-form approximations derived previously. The resulting formulas provide practical guidelines for predicting the peak RCS, envelope width, and grating-lobe locations.

By analyzing (39)–(45) for Geometry 1 and considering a large rectangular mosaic array of size $L_x \times L_y$ with $N \gg 1$, $M \gg 1$, and $a \gg \lambda_0$, several key array characteristics can be identified.

- **Peak RCS.** The peak array RCS is equal to the single-reflector RCS multiplied by the square of the element count:
$$\sigma^{\max} = \sigma_0 (NM)^2.$$
Expressed using the physical aperture $L_x = (M/2)\, d_{x1}$ and $L_y = N\, d_{y2}$:
$$\sigma^{\max} = \frac{4\pi}{\lambda_0^2}(L_x L_y \eta)^2,$$
where η is the aperture-usage efficiency. For a contiguous mosaic array, $\eta = 2/3$, which is equal to that of a single trihedral. With gaps included,
$$\eta = \frac{\frac{2}{3}(a^2\sqrt{3})MN}{L_x L_y} = \frac{4}{3}\frac{a^2\sqrt{3}}{d_{x1} d_{y2}},$$
where d_{x1} and d_{y2} increase if spacing is introduced.

  As the electrical size of individual trihedral corner reflectors decreases, the scattering mechanism transitions from corner-reflector-dominated behavior to aperture-dominated, flat-plate-like scattering. In this regime, the retroreflective gain of individual elements is reduced. However, for sufficiently large mosaic arrays composed of electrically small reflectors, the overall RCS scaling remains governed by the physical aperture of the array, explaining the plate-like scattering behavior and predictable array-level RCS characteristics.

  As can be seen from Fig. 14(b), in the regime $a \ll \lambda_0$ and $M \gg 1$, $N \gg 1$, the peak RCS can be estimated by assuming an aperture-usage efficiency $\eta \approx 1$, analogous to that of a flat metallic plate. In this limit, the scattering behavior of the array becomes aperture-dominated rather than corner-reflector-dominated. In addition, the sidelobe structure observed in Fig. 14(b) indicates that the proposed array-factor-based formulation, together with (34), can be extended to estimate the RCS of targets with more complex geometries. A complex object may be approximated as an array of small flat reflector elements with area A_f and individual RCS $\sigma_{\mathrm{f}} = \frac{4\pi}{\lambda_0^2} A_f^2$. The total RCS can then be estimated by applying the array-factor approach and integrating the contributions over the entire surface.
- **Envelope width.** The angular envelope of the array RCS is governed by the single-TCR pattern from (19)–(26). The main envelope width is approximately 40° at the -3 dB level in both principal planes, consistent with Fig. 11 and classical Refs. [15, 16, 18].
- **Main-lobe width.** From (39) and (45), the half-power widths of the primary grating lobes are
$$2\theta_{0.5}|_{\varphi=0} \approx 0.44\frac{\lambda_0}{L_x}, \quad 2\theta_{0.5}|_{\varphi=\pi/2} \approx 0.44\frac{\lambda_0}{L_y}.$$
These results agree with the standard aperture formulas [11, 12]. Owing to the doubled optical path in monostatic scattering, the array grating lobes are approximately twice as narrow as those of a conventional antenna array.
- **Grating-lobe angles for $\varphi = 0$.** For the xz-plane:
$$\theta_m|_{\varphi=0} = \arcsin\left(\pm\frac{\lambda_0}{2d_{x1}}m\right), \quad m = 0, 1, 2, \ldots,$$
from (39).
- **Grating-lobe angles for $\varphi = \pi/2$.** For the yz-plane:
$$\theta_n|_{\varphi=\pi/2} = \arcsin\left(\pm 3\frac{\lambda_0}{2d_{y1}}n\right), \quad n = 0, 1, 2, \ldots.$$
The modulation term $\cos(\Psi_{y1}/12)$ in (45) attenuates approximately two-thirds of the grating lobes and increases the spacing between the dominant lobes by a factor of three. The suppressed lobes were reduced by approximately 6 dB.

These characteristics are illustrated in Fig. 18.

For dielectric TCRAs, the analytical framework should be interpreted as an array-level approximation rather than a fully independent dielectric scattering model. While the metal-array formulation accurately predicts grating-lobe locations and aperture-controlled scaling, the strongly non-symmetrical patterns and reversed boresight offsets observed in dielectric arrays arise from internal refraction and multiple reflections that require full-wave analysis. A closed-form analytical model explicitly accounting for these dielectric effects remains an open research problem.

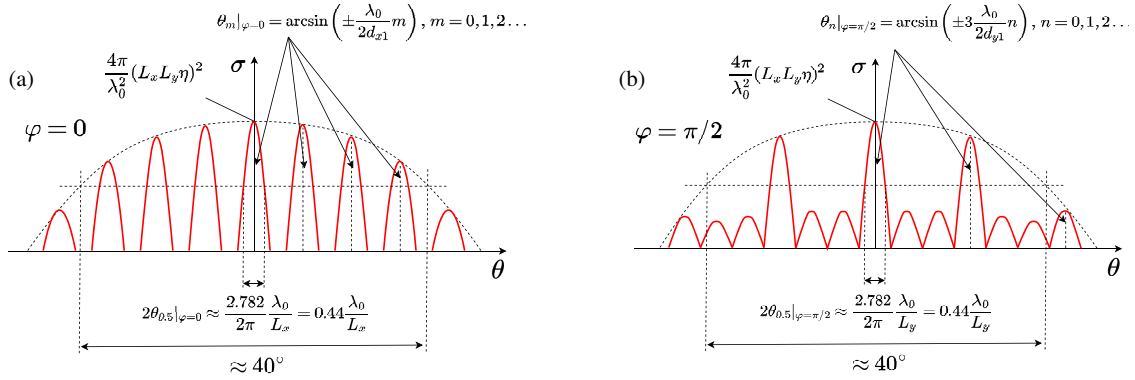

FIGURE 18. Estimation of main parameters of the monostatic RCS of a TCRA. $M \gg 1$, $N \gg 1$, $a \gg \lambda_0$. (a) $\varphi = 0$ (xz-plane), using Eq. (39); (b) $\varphi = \pi/2$ (yz-plane), using Eq. (45).

TABLE 1. Comparison of analytical and numerical modeling approaches for corner reflectors and array-level scattering formulations.

Reference	Target Type	Geometry	Method	Closed-Form (General)	Closed-Form (Simplified)	TCR Orientations	Polarization Analysis	Material	Validation
[8]	Single TCR	Isolated	GO	Yes	-	-	No	Metal	Numerical
[13]	Single TCR (extended plate)	Isolated	GO	Yes	-	-	No	Metal	Simulation (SAF) + Measurement
[15]	Single TCR	Isolated	GO-PO-PO	No	No	-	No	Metal	Simulation + Measurement
[19]	Single TCR	Isolated	GO + Gordan surface integral method	Yes	No	-	No	Metal	Simulation (FEKO)
[6]	Single TCR	Isolated	PO-SBR	No	No	-	Yes	Metal	Simulation (FEKO)
[4]	TCRA (3D)	Great-icosahedral-like array	GO + AF	Yes	No	Yes	Yes	Metal	Simulation (FEKO)
[5]	TCRA (3D)	Airborne reflector array	GO + AF	Yes	No	Yes	No	Metal	Simulation (FEKO + CST)
[9]	TCRA (2D)	Mosaic array (4 TCRs)	Simulation TCR + AF	No	No	No	No	Dielectric	Simulation (CST)
[20]	Circular elements array (2D)	Hexagonal array	AF	No	Yes	No	No	Metal (sound sources)	-
[7]	Vivaldi antenna array (2D)	Planar array	AF	Yes	No	No	No	Metal	Simulation (HFSS) + Measurement
This work	TCR/TCRA (2D)	Mosaic array	GO + AF	Yes	Yes	Yes	No	Metal/ Dielectric	Simulation (COMSOL) + Measurements ([9])

Table 1 summarizes representative analytical and numerical approaches for modeling the radar cross section of trihedral corner reflectors and related array-level scattering problems, including non-corner-reflector arrays as methodological references for array-factor-based formulations. Here, "Closed-Form (General)" denotes explicit summation-based analytical expressions, while "Closed-Form (Simplified)" refers to reduced approximations with direct dependence on physical array parameters.

As shown, the present work extends classical GO-based and array-factor formulations to mosaic array configurations while retaining closed-form analytical tractability.

12. CONCLUSION

This study presents a unified analytical and numerical study of the monostatic radar cross section (RCS) of trihedral corner reflectors (TCRs) and their arrays (TCRAs), combining geometrical-optics (GO) formulations with full-wave simulations using the Finite Element Method (FEM) in COMSOL Multiphysics. A comparison between the closed-form expressions and numerical simulations established the validity range of the GO-based models and quantified the physical effects that arise when the reflector size becomes comparable to the wavelength.

For single TCRs, analytical predictions closely match FEM simulations when the reflector is electrically large ($a \gg \lambda_0$). As the reflector size decreases toward $a \approx \lambda_0$, diffraction and internal resonance effects introduce additional lobes, asymmetries, and phase distortions that are not captured by the GO expressions. When $a \ll \lambda_0$, the RCS becomes nearly omnidirectional and remains surprisingly high, demonstrating that small TCRs can still act as effective scattering elements even though aperture-based formulas are no longer valid.

For TCRAs, analytical expressions based on array-factor multiplication show good agreement with FEM simulations when $a \geq \lambda_0$. Deviations occur when the element dimensions approach the wavelength, where edge diffraction, mutual coupling, and phase distortion become significant. Geometry 1 (dual-plane symmetry) enables substantial reductions in the FEM computational cost. Large arrays with $L_x, L_y \gg \lambda_0 \gg a$ exhibit scattering behavior similar to that of a metallic plate with the same physical aperture, confirming the scalability of the array-factor formulation.

The measured data for the dielectric four-element TCRA reported in [9] were also used for the validation. The FEM simulations and analytical model reproduced the key measured features in the $\varphi = 0$ plane and correctly predicted the strong nonsymmetry observed in the $\varphi = \pi/2$ plane. This confirms that the proposed analytical formulation remains applicable to dielectric reflector arrays, despite the additional complexities introduced by refraction and internal reflections.

Limitations: The analytical models rely on GO assumptions, which are valid primarily for electrically large reflectors and non-grazing incidence. For $a \lesssim \lambda_0$, the FEM results reveal diffraction, edge scattering, mutual coupling, and internal resonance phenomena that are not represented in the GO-based closed-form expressions. The analysis also assumes negligible mutual coupling between neighboring TCRs, an approximation that becomes less accurate for tightly packed arrays. Additional discrepancies arise from numerical factors in the FEM environment, such as the PML shape, finite computational domains, and mesh coarsening in multi-scale problems. Therefore, the COMSOL simulations conducted in this study were used to identify and quantify these validity limits.

The analytical formulation also assumes purely co-polar scattering, whereas the total RCS extracted from the FEM simulations includes any cross-polarization arising from finite edges, dielectric loading, and multi-bounce interactions. These effects are small for metallic reflectors [6] but are more pronounced in dielectric TCRs and tightly packed arrays.

Overall, this study demonstrates that GO-based formulations provide accurate and computationally efficient predictions for electrically large TCRs and TCRAs. However, for intermediate and small reflector sizes, phase distortions and wave-interaction effects must be considered to ensure an accurate RCS prediction. The derived expressions provide practical design guidelines: the peak RCS scales with the physical aperture of the array, the angular envelope is governed by the single-TCR pattern, and the grating-lobe widths are narrower than those in conventional antenna arrays owing to the doubled propagation path. In the $\varphi = \pi/2$ plane, additional modulation attenuates the secondary lobes and widens their spacing.

The differences observed between the metal and dielectric TCRAs, particularly in the $\varphi = \pi/2$ plane, highlight the influence of material properties on the scattering behavior. Future work should extend the analytical model to include vector-field polarimetric effects, coupling-aware formulations, and hybrid GO-wave models to improve the accuracy for electrically small and dielectric reflector arrays. The COMSOL simulation files supporting this study are available in the Data Availability section.

13. FUTURE WORK

The results of this study suggest several promising directions for further research:

- **Material properties and fabrication tolerances.** The present analysis assumes perfectly conducting reflectors to be present. Future work should investigate the impact of finite conductivity, surface roughness, geometric tolerances, and nonuniform or near-field incident wavefronts on the RCS performance, particularly for electrically small reflectors, where losses and imperfections are more influential. The effects of positioning errors and assembly tolerances in mosaic arrays also warrant systematic studies.
- **Experimental validation of the proposed model.** Laboratory or outdoor measurements of individual TCRs and TCRAs would provide essential validation of the analytical models and FEM simulations. Such measurements would also help quantify the influence of practical factors, such as edge rounding, assembly misalignment, and environmental contributions.
- **Array geometry and configuration.** Beyond regular rectangular arrays, future investigations should consider nonuniform, sparse, or adaptive reflector arrangements. Hybrid structures that combine corner reflectors with other scatterers can also be explored for tailored RCS shaping and improved angular coverage.
- **Phase-aware single-reflector model.** The phase distortions observed for finite a/λ_0 suggest the need for refined analytical models incorporating diffraction and resonance effects. Future models should add angle-dependent phase terms to Eqs. (19) and (26) and account for side "ears" caused by flat-plate single-bounce contributions. Such improvements would enhance the array-level accuracy of electrically small and intermediate-size reflectors.

- **Polarimetric and scattering-matrix formulations.** Extending the present scalar RCS framework to a polarimetric scattering-matrix formulation would enable the explicit treatment of phase and cross-polarization effects in TCRAs and is particularly relevant for radar calibration. A further extension is a hybrid numerical-analytical approach combining numerically computed single-reflector responses (e.g., [9]) with analytical array-factor models, generalized to multiple orientations and dielectric materials.
- **Computational optimization.** Work on efficient meshing strategies, advanced PML configurations, and high-performance FEM solvers could further reduce the computational cost. This enables an accurate full-wave simulation of very large arrays with practical geometries.
- **Dielectric reflector arrays.** Several research directions have emerged for dielectric TCRAs. A parametric study of the dielectric properties (ε_r, $\tan\delta$) should be conducted to quantify their influence on the RCS trends. Internal multiple reflections and refractions can be explored using improved FEM models or ray-tracing techniques. Experimental validation for both $\varphi = 0$ and $\varphi = \pi/2$ planes would be especially valuable. Optimization strategies, including material selection and geometric adjustments, may help reduce asymmetry and improve the peak RCS.
- **Coupling-aware and diffraction-corrected analytical models.** A promising direction is the incorporation of mutual-coupling effects and diffraction-corrected single-element responses into the array formulation. Such enhancements would significantly improve the prediction accuracy for tightly packed or electrically small TCRAs.

DATA AVAILABILITY

The supplementary materials and datasets supporting the results of this work are publicly available at IEEE Dataport (DOI: https://dx.doi.org/10.21227/cr1x-ra35) and Figshare (DOI: https://doi.org/10.6084/m9.figshare.30874823.v1).

REFERENCES

[1] Hockel, H., R. F. Martins, J. Sung, and E. G. Johnson, "Design and fabrication of trihedral corner-cube arrays using analog exposure based on phase masks," in *Proc. SPIE 5720, Micromachining Technology for Micro-Optics and Nano-Optics III*, Vol. 5720, 78–85, San Jose, California, USA, 2005.

[2] Brinksmeier, E., R. Gläbe, and C. Flucke, "Manufacturing of molds for replication of micro cube corner retroreflectors," *Production Engineering*, Vol. 2, No. 1, 33–38, 2008.

[3] Gao, J., Y. Lei, and Z. Xu, "Research on micro-triangular pyramid array-based fly-cutting technology using the orthogonal test method," *Coatings*, Vol. 14, No. 7, 806, 2024.

[4] Wu, L., J. Xu, S. Hu, and Z. Liu, "High-frequency backscattering properties of quasi-omnidirectional corner reflector: The great-icosahedral-like reflector," *AIP Advances*, Vol. 12, No. 10, 105225, 2022.

[5] Wu, L., S. Hu, J. Xu, and Z. Liu, "Dynamic sequential radar cross section properties of airborne corner reflector in array," *IET Radar, Sonar & Navigation*, Vol. 17, No. 9, 1405–1419, 2023.

[6] He, Y., H. He, C. Hu, J. Yin, and J. Yang, "Polarization analysis of trihedral corner reflector with high-frequency approximation," *IEEE Transactions on Antennas and Propagation*, Vol. 70, No. 10, 9607–9620, 2022.

[7] Gou, Y., Y. Chen, and S. Yang, "Radar cross section reduction of wideband Vivaldi antenna arrays with array-level scattering cancellation," *IEEE Transactions on Antennas and Propagation*, Vol. 70, No. 8, 6740–6750, 2022.

[8] Groot, J., "Letter: Cross section computation of trihedral corner reflectors with the geometrical optics approximation," *European Transactions on Telecommunications*, Vol. 3, No. 6, 637–642, 1992.

[9] Buchberger, C., F. Pfeiffer, and E. Biebl, "Dielectric corner reflectors for mmWave applications," *Advances in Radio Science*, Vol. 17, 197–203, 2019.

[10] Skolnik, M. I., *Introduction to Radar Systems*, 2nd ed., McGraw-Hill, New York, 1980.

[11] Shyfryn, Y. S., *Antenny [Antennas]*, VYRTA im. L. A. Hovorova, Kharkov, Ukraine, 1976.

[12] Balanis, C. A., *Antenna Theory: Analysis and Design*, 3rd ed., Wiley, Hoboken, NJ, USA, 2005.

[13] Doerry, A. W. and B. C. Brock, "Radar cross section of triangular trihedral reflector with extended bottom plate," in *Sandia Report*, Sandia National Laboratory, 2009.

[14] Ruck, G. T., *Radar Cross Section Handbook*, Plenum Press, New York, NY, USA, 1970.

[15] Sarabandi, K. and T.-C. Chiu, "Optimum corner reflectors for calibration of imaging radars," *IEEE Transactions on Antennas and Propagation*, Vol. 44, No. 10, 1348–1361, 1996.

[16] Crispin, J. W. and K. M. Siegel, *Methods of Radar Cross-Section Analysis*, Academic Press, New York, NY, USA, 1968.

[17] Korn, G. A. and T. M. Korn, *Mathematical Handbook for Scientists and Engineers*, Dover/Courier, Mineola, NY, USA, 2000.

[18] Skolnik, M. I., *Radar Handbook*, 3rd ed., McGraw Hill, New York, NY, USA, 2008.

[19] Weng, Y.-K., S. Li, J.-L. Yang, H. Zhou, H. Yi, and H. Wang, "Efficient solution to the RCS of trihedral corner reflector," *International Journal of Applied Electromagnetics and Mechanics*, Vol. 47, No. 2, 533–539, 2015.

[20] Yokoyama, T., T. Asami, K. Mori, and A. Hasegawa, "Radiation characteristics of hexagonal transducer array," *Japanese Journal of Applied Physics*, Vol. 44, No. 6S, 4702, Jun. 2005.

[21] COMSOL Multiphysics®, "Comsol multiphysics v. 6.4," https://www.comsol.com, cOMSOL AB, Stockholm, Sweden, 2025.

[22] Knott, E. F., *Radar Cross Section Measurements*, Springer, New York, NY, USA, 2012.